

Chemistry

Special Topic: Chemistry Boosts Carbon Neutrality

Hydroformylation over polyoxometalates supported single-atom Rh catalysts

Shixiang Feng¹, Qi Yu^{2,*}, Xinbin Ma^{1,3}, Xiaohu Yu² & Ning Yan^{1,4,*}¹Joint School of National University of Singapore and Tianjin University, International Campus of Tianjin University, Binhai New City, Fuzhou 350207, China;²School of Materials Science and Engineering, Shaanxi Laboratory of Catalysis, Shaanxi University of Technology, Hanzhong 723001, China;³School of Chemical Engineering and Technology, Tianjin University, Tianjin 300072, China;⁴Department of Chemical & Biomolecular Engineering, National University of Singapore, Singapore 117580, Singapore*Corresponding authors (emails: qiyu@snut.edu.cn (Qi Yu); ning.yan@nus.edu.sg (Ning Yan))

Received 30 September 2022; Revised 3 February 2023; Accepted 6 February 2023; Published online 28 February 2023

Abstract: Atomic dispersion of Rh on phosphotungstic acid (PTA) salts was achieved by a self-assembled precipitation method using alkali metal ions as coprecipitation reagents. During styrene hydroformylation, the supported Rh single-atom catalyst (Rh₁/M-PTA, M refers to an alkali metal ion) demonstrated an optimum turnover frequency (TOF) of 1076 h⁻¹. With increasing ionic radius, the pore size of the catalysts increased in the following order: Rh₁/K-PTA < Rh₁/Rb-PTA < Rh₁/Cs-PTA. The catalytic activity showed the same trend, suggesting a positive correlation between pore size and hydroformylation performance. Further experimental data suggested that temperature is an important factor affecting not only the activity but also the selectivity. This study enriches the understanding of the structure and catalytic properties of PTA-supported single-atom materials. The cation-controlled synthesis of catalysts may also be applied to prepare other single-atom catalysts with tunable pore size distributions.

Keywords: polyoxometalates, Rh single-atom, hydroformylation, self-assembly, styrene

INTRODUCTION

The hydroformylation of olefins to aldehydes is among the largest industrial reactions promoted by homogeneous catalysts [1], enabling the functionalization of olefins and the growth of the carbon chain. It opens up paths towards a broad range of value-added downstream products such as amines, alcohols, esters, and carboxylic acids [2]. Despite their excellent activity and selectivity, traditional homogeneous rhodium catalysts are not easily recyclable and not sufficiently stable. Efforts have been made to immobilize rhodium complexes onto solid supports for easy separation, in which Rh species are still coordinated with organic ligands [3–6]. Alternatively, a phosphine ligand can be added in the postsynthesis stage to modulate Rh species on solid supports owing to its firm metal-ligand coordination [7]. After P doping, Rh exhibited excellent stabilization and enhanced regioselectivity through geometric and electronic effects [8,9].

Organic ligand-free single-atom catalysts (SACs) represent a new class of materials with multiple applications in catalysis [10–18]. Much progress has been made in unsaturated chemical hydrogenation [19–33], organic chemical oxidation [34–39], CO₂ conversion [40–46], CO oxidation [47–56], biomass conversion [21,31,57–59], etc. Different supported Rh single-atom catalysts have also shown promising hydroformylation activity [60–65]. By depositing Rh onto the vacancies on ZnO nanowires (Rh₁/ZnO-nw) [60] and CeO₂ (Rh₁/CeO₂) [62,63] or replacing Co atoms with Rh on CoO nanosheets (Rh₁/CoO) [61], the atomic dispersion of Rh was achieved with enhanced catalytic performance. Due to the strong metal-support interaction and unique local chemical environment, the Rh single-atom catalysts exhibited similar or even higher efficiency compared with the homogeneous Wilkinson's catalyst and can also be reused with no significant loss of activity and selectivity. In addition to the metal oxide supports, a manganese-based metal organic framework (MOF)-incorporated Rh was designed and used for styrene hydroformylation at 80°C with high selectivity, high catalyst recyclability, and negligible metal leaching [66]. When ionic liquids (ILs) were added as extra protecting reagents, the Rh₁/TiO₂ catalyst demonstrated greatly enhanced stability without compromising activity [67] (turnover frequency, TOF = 878 h⁻¹). After five runs, the TOF value was only slightly reduced by 9% to 800 h⁻¹ during styrene hydroformylation. In a more recent study of the same reaction, Rh-substituted polyoxometalate-based ILs achieved ultrahigh activity (TOF > 9000 h⁻¹) [65]. Polyoxometalates (POMs) with quaternary ammonium cations showed a low melting point and behaved as homogeneous catalysts under reaction conditions.

Among various supports, POMs, as molecularly defined metal-oxo clusters, have been extensively used to prepare SACs with uniform structures. POMs only exhibit a limited number of binding sites for atomically dispersed metals such as Pt, Pd, or Rh, thus representing ideal systems for investigating the working mechanism of active sites on SACs. Previously, we studied CO and alcohol oxidation reactions [50,52,54,56], the hydrogenation of various unsaturated compounds [20], and the hydrogen spillover phenomenon and its correlation to catalysis [29]. Since the surface area of the parent molecule of POMs, usually referring to protonated heteropoly acids, is small and thus not suitable to be directly used as supports, two methods are used to increase their dispersion: (1) the anchoring of POMs on high surface area supports, such as carbon; (2) the formation of porous POM salts through ion exchange between protons and inorganic metal cations. The parent structure, comprising Keggin-type anions, formed new oriented and crystalline POM salts possessing larger pores and skeletons after the replacement of the original H₅O₂⁺ by cations (Cs⁺, NH₄⁺, etc.), which to a large extent increased the specific surface area (from ~10 to ~100 m²/g) and pore size and therefore promoted the dispersion of metals. In this work, we prepared Rh₁-doped, porous POM salts containing different cations and with pore sizes by a self-assembled precipitation method. Catalytic performance was evaluated under different conditions to probe structure-activity correlations.

EXPERIMENTAL

Catalyst preparation

The catalysts were synthesized by self-assembly through a typical procedure as follows. A specific amount of Rh(NO₃)₃ stock solution (Rh conc. = 1178.4 mg/L) was mixed with an aqueous solution of phosphotungstic acid (PTA) for 4 h at room temperature. Then, stoichiometric amounts of dissolved nitrates (CsNO₃, RbNO₃,

KNO_3) were added dropwise to the above mixture under vigorous stirring (600 r/min) for 20 min to form a white colloidal solution. After further stirring for 1 h, the generated precipitates were centrifuged (8000 r/min, 10 min) and thoroughly washed to remove nitrate residues. After drying at 333 K overnight, the solids were ground, followed by calcination at 523 K for 30 min under flowing air. The obtained catalyst was denoted as $x\text{Rh}/\text{M}-\text{PTA}$ (where x represents weight percentage and M refers to the alkali metal cation Cs, Rb, or K).

Rh_1/TiO_2 , Rh_1/CeO_2 and Rh_1/ZrO_2 with 0.1 wt% loadings of Rh were prepared by a simple impregnation method. In a typical procedure, stoichiometric amounts of $\text{Rh}(\text{acac})(\text{CO})_2$ were dissolved in 10 mL of acetone, and 1 g of support (TiO_2 , CeO_2 , ZrO_2) was added to the above Rh precursor solution. The obtained mixture was stirred in open air at room temperature until the solvent evaporated completely. Then, the obtained powder was calcined at 200°C for 1 h in air.

Catalyst characterization

The Rh contents in the catalyst samples were determined by inductively coupled plasma-mass spectrometry (ICP-MS) on an Agilent ICP-MS 7800 after microwave digestion. X-ray diffraction (XRD) patterns were obtained on a powder X-ray diffractometer (SmartLab, Rigaku) using $\text{Cu K}\alpha$ radiation ($\lambda = 1.5405 \text{ \AA}$). Scanning electron microscopy (SEM) observations were conducted on a Hitachi Regulus 8100 instrument. The samples were first dispersed in ethanol and dropped onto a supported conductive adhesive. After solvent evaporation, the sample was treated by gold sputtering before SEM observation. Transmission electron microscopy (TEM) images were acquired using a JEOL JEM-F200 instrument. The samples were first dispersed in ethanol, after which a small amount of suspension was dropped onto carbon-coated copper grids followed by drying in air overnight. Element mapping was also conducted.

The specific surface areas and pore size distributions were estimated based on data acquired from a N_2 adsorption analyser (BELSORP-max, MicrotracBEL). Prior to analysis, each sample was evacuated at 473 K for 2 h. N_2 isotherms obtained at 77 K were analysed using the Horvath-Kawazoe (HK) method. CO-diffuse reflectance infrared Fourier transform (CO-DRIFT) spectra were acquired using an FTIR spectrometer (iS50 FT-IR, NICOLET) equipped with a liquid N_2 cooled MCT detector and a DRIFT chamber (DRK-4-NI8, HARRICK). Prior to each analysis, the sample was pretreated under Ar flow (40 mL/min) at 473 K for 30 min and then cooled to room temperature. After supplying a CO/Ar mixture flow (6:60, v/v) to the cell for 20 min, spectra were recorded over 1 h while keeping the cell at 323 K to remove physically adsorbed CO.

X-ray adsorption spectra at the Rh K-edge were obtained on the BL01B1 beamline at the SPring-8 facility (Japan) operating in both fluorescence and transmittance modes. An electron beam energy of 8 GeV was used together with a Si (311) two-crystal monochromator.

Catalytic activity evaluation

The hydroxylation reaction was conducted in a sealed autoclave with a Teflon tube embedded inside. In a typical procedure, 20 mg catalyst was added to the tube, followed by introducing 2 mmol styrene and 3 mL toluene. After charging 2 MPa syngas ($\text{H}_2:\text{CO} = 1:1$) into the autoclave, the sealed reactor was placed in the heater at the set temperature with vigorous stirring, and then the hydroformylation reaction started. At

different time intervals, the reaction mixture was filtered prior to gas chromatography (GC) analysis using hexane as an internal standard.

$$\text{Conversion \%} = \text{converted substrates (mol)} / \text{total substrate (mol)} \times 100\%.$$

$$\text{Selectivity \%} = \text{obtained products (mol)} / \text{total substrate (mol)} \times 100\%.$$

TOF (h^{-1}) = converted substrates (mol)/[total metal (mol) \times reaction time (h)]; TOF was calculated based on low conversion (<15%). For better comparison, the specific reaction times were 2, 5 and 10 h for Rh₁/Cs-PTA, Rh₁/Rb-PTA, and Rh₁/K-PTA, respectively.

Calculation details

The theoretical calculations were performed by using the spin-polarized Kahn-Sham formalism of density functional theory (DFT) via the Vienna *ab initio* simulation package (VASP) [68]. The Perdew-Burke-Ernzerhof (PBE) exchange-correlation functional of the generalized gradient approximation (GGA) was adopted [69]. Projector augmented-wave (PAW) potentials with scalar-relativistic effects were used to account for the interaction between the valence electrons and ionic core with the nucleus [70,71]. A cut-off energy of 420 eV was used for the plane wave expansion. The geometries were optimized with the self-consistent field energy converged to 10^{-5} eV, and the force convergence criteria were set to 0.02 eV/Å.

RESULTS AND DISCUSSION

Structure and texture of the catalyst

In the preparation process, the Rh³⁺ and phosphotungstate anions (PW₁₂O₄₀³⁻) formed a neutral complex (Rh₁PTA₁) in a one-to-one manner [53]. By precipitating PW₁₂O₄₀³⁻ in solution with K⁺, Rb⁺ and Cs⁺, self-assembled Rh/M-PTA (M refers to Cs, Rb, or K) particles were subsequently obtained (Scheme S1). As shown in the SEM image, the particle size of the catalyst was distributed in the range of 100–200 nm (Figure 1A). Misono *et al.* [72] proposed that spherical self-assembled solids had three classes of structures, consisting of phosphotungstate anions (primary structure), ionic crystals (secondary structure), and assembled spherical porous particles (tertiary structure). In this study, rough surfaces with small aggregates were clearly observed because different crystalline grains tended to aggregate to form roughly round particles due to molecular cohesion in the aqueous solution (tertiary structure, Figure 1B). The ionic crystals had a cubic structure consisting of monovalent metal cations (K⁺, Rb⁺, Cs⁺) and PW₁₂O₄₀³⁻ after the ion exchange of protons (secondary structure, Figure 1C). In our previous work, based on extended X-ray absorption fine structure (EXAFS) data and DFT calculations, the Pt atoms [20,50] and Rh atoms [52] were most stable when located at 4-fold hollow sites on the POMs due to firm coordination. EXAFS spectra for the as-prepared samples were also provided in the present work. As shown in Figure S1, the intensity of Rh/Cs-PTA was similar to that of Rh₂O₃. According to the XANES, no Rh–Rh bond contribution was observed, indicating that Rh only existed in isolated Rh(III) species coordinated with O. The Rh–O shell fitting results are listed in Table S1. The Rh–O bond length and coordination number were calculated to be 2.02 Å and an average of 5.6, respectively.

The optimized geometry of Rh₁/PTA is shown in Figure 1D. For the surface atoms of the Keggin-type

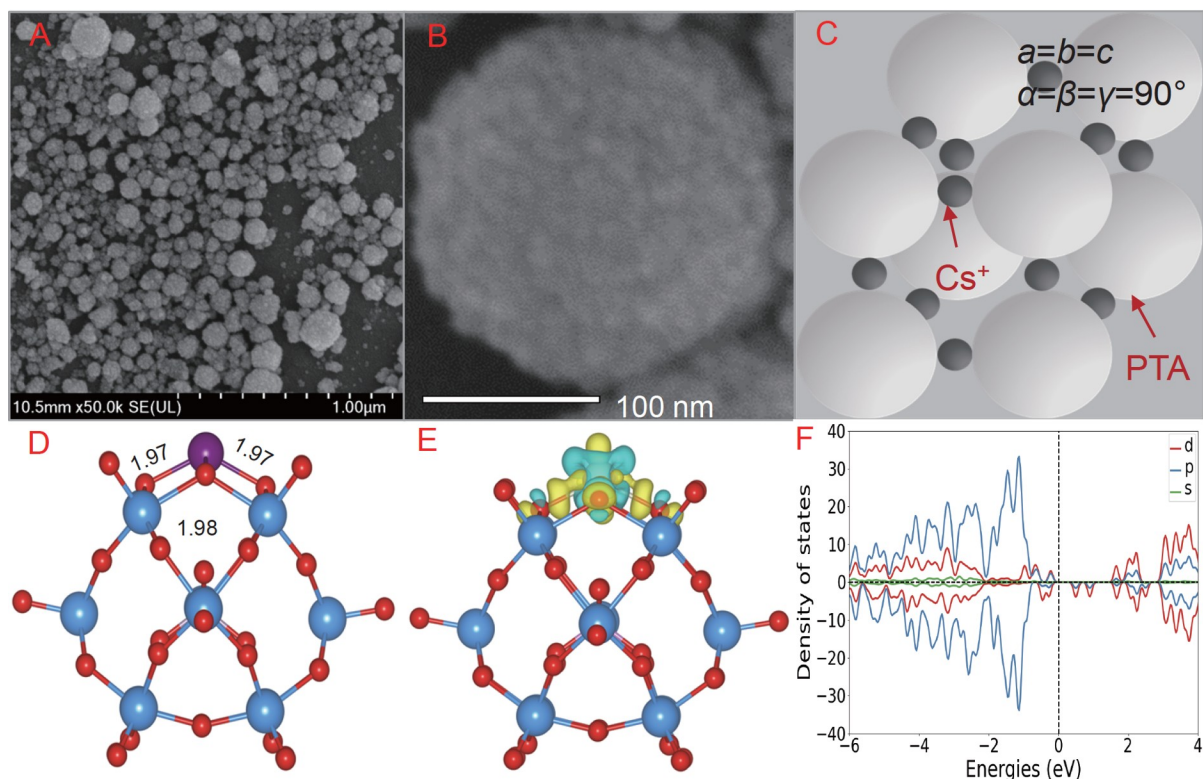


Figure 1 (A) SEM image of Rh1/Cs-PTA. (B) Tertiary structure: porous particle (100–200 nm). (C) Secondary structure: ionic crystals (10–20 nm). (D) Primary structure: top view of the optimized geometry of Rh1/PTA, ~1 nm, purple: Rh, blue: W, red: O, pink: P. (E) Charge density difference of Rh1/PTA. (F) Spin-polarized partial density of states projected on Rh s, p and d (green, blue and red) states.

structure, the bridges (O_b) and sides of the Keggin structure (O_c) were suitable anchoring sites for an isolated single metal atom. The Rh atom preferred to bind at the 4-fold hollow site of the PTA cluster, with a calculated binding energy of -2.48 eV. The optimized $W-O_c$ and $W-O_b$ bond lengths were 1.98 and 1.97 Å, respectively, indicating significant binding of a Rh single atom on the surface. The calculated bond angle of $W-O_c-W$ (123°) was smaller than that of $W-O_b-W$ (141°). The optimized Co_1/PTA and Ir_1/PTA catalysts are also shown in Figure S2. To gain more insight into the nature of the chemical bonding of Rh1/PTA, the charge density difference (CDD) was calculated. As shown in Figure 1E, there was a clear loss of electron density from the Rh atom, which implied that the electron density flowed from Rh to the nearest O atoms in Rh1/PTA. This charge transfer from the Rh centre to the Keggin-type PTA cluster cage caused ionic interactions between Rh and O atoms, which mainly accounted for the large binding energy of Rh [73]. The Bader charge of Rh1 in M_1/PTA is $+1.17|e|$. We further studied the spin-polarized partial density of states (PDOS), as shown in Figure 1F. The spin-up and spin-down PDOS of the Rh 4d orbitals were asymmetric near the Fermi level, indicating the spin polarization of Rh. The presence of Rh 4d-based quantum states near the Fermi level resulted in high activity towards small molecules and may have played a role in activating the adsorbates during the catalytic reaction.

According to the N_2 adsorption-desorption results, the catalyst had micropores ranging from 0.5 to 2 nm (Figure 2). The peak centred at 0.56 nm was attributed to the ordered pores in crystals, which depended on

the size of the cations. With increasing ion size ($K^+ < Rb^+ < Cs^+$), the micropores grew larger (Scheme S2). Additionally, there was a micropore distribution ranging from 0.6 to 2 nm, which was ascribed to the irregular slits between different crystals within the spherical particle (Figure 1C). In addition, the specific areas were calculated based on the N_2 adsorption-desorption results. When protons were replaced by K^+ , the specific area increased from <10 to $147 \text{ m}^2/\text{g}$. With increasing cation size, the specific areas of Rh_1/Rb -PTA and Rh_1/Cs -PTA were determined to be 163 and $160 \text{ m}^2/\text{g}$, respectively.

XRD patterns were recorded and are shown in Figure 2. The structure of the Keggin anion was well preserved in all samples. There was a significant shift of the crystalline peak to a small diffraction angle with increasing cation size. Brown *et al.* [74] confirmed the hexahydrate formula of $(H_5O_2^+)_3(PW_{12}O_{40}^{3-})$ through X-ray and neutron single-crystal diffraction methods. The six water molecules were paired in nearly planar diaquahydrogen ions of $H_5O_2^+$. After the hydrated proton ($H_5O_2^+$) was replaced by K^+ , Rb^+ , or Cs^+ , the lattice constants of Rh_1/K -PTA, Rh_1/Rb -PTA and Rh_1/Cs -PTA decreased to 11.59 , 11.68 , and 11.92 \AA , respectively. As a reference, the lattice constant was 12.16 \AA when the hydrated proton ($H_5O_2^+$) acted as the counter cation.

The element mapping image indicated that W, Cs, and Rh had high spatial correlation, demonstrating the

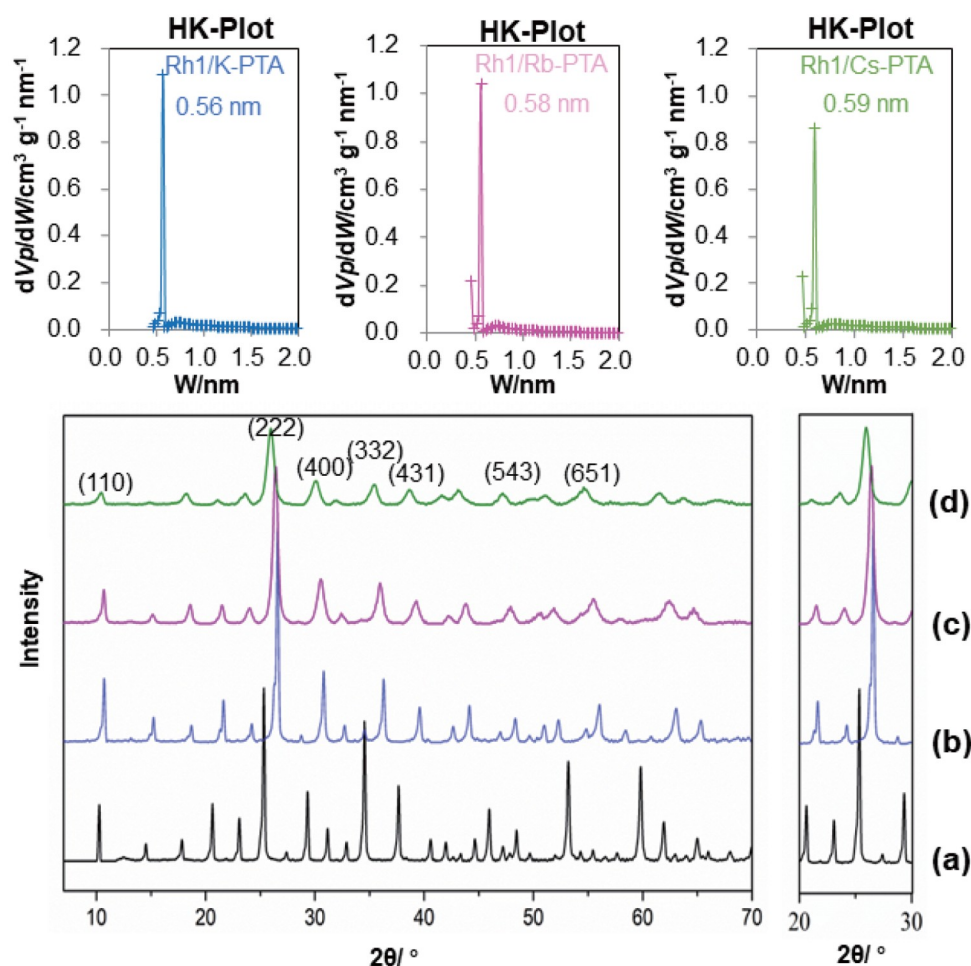


Figure 2 (Upper) HK-plot analysis of N_2 adsorption-desorption isotherms. (Lower) XRD patterns of Rh_1/H -PTA (a), Rh_1/K -PTA (b), Rh_1/Rb -PTA (c), and Rh_1/Cs -PTA (d).

uniform Cs-PTA structure and evenly distributed Rh (Figures 3A–3C). In the CO-DRIFT spectra (Figure 3D), two IR peaks at approximately 2110 and 2050 cm^{-1} were associated with the symmetric and asymmetric stretches of the positively charged $\text{Rh}(\text{CO})_2$ gem-dicarbonyl species [75], demonstrating that Rh metals were atomically dispersed on the supports.

Hydroformylation activities

Due to the different solubilities of PTA salts ($\text{K-PTA} > \text{Rb-PTA} > \text{Cs-PTA}$) [72], fine particles were formed at different precipitation rates after the addition of cations into the PTA solution. As mentioned in the catalyst preparation section, $\text{Rh}(\text{NO}_3)_3$ was first mixed with an aqueous solution of PTA to form the $\text{Rh}_1\text{-PTA}_1$ complex through electrostatic interactions. Then, after the addition of cations (Cs^+ , Rb^+ , K^+), the cation-PTA grains quickly precipitated due to their low solubility. During this self-assembly process, the initially formed $\text{Rh}_1\text{-PTA}_1$ complex could probably be coprecipitated and finally enclosed by the numerous crystal grains and

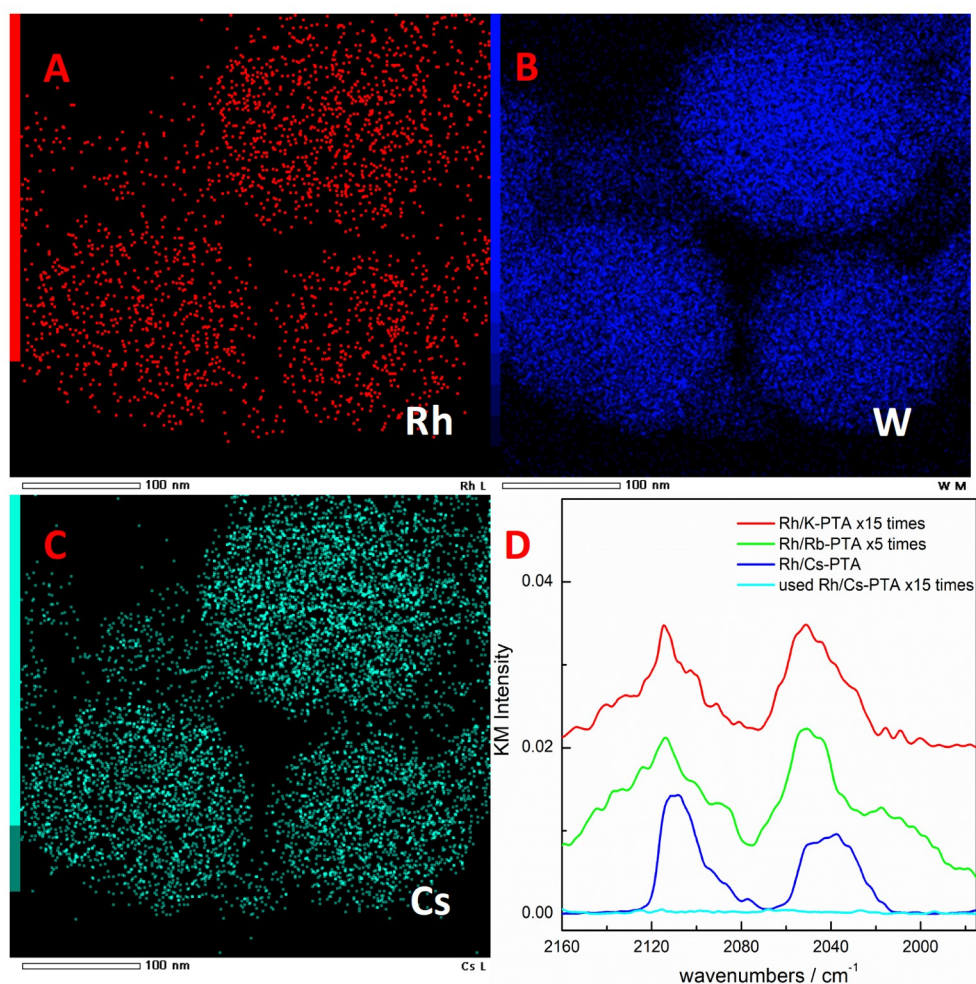
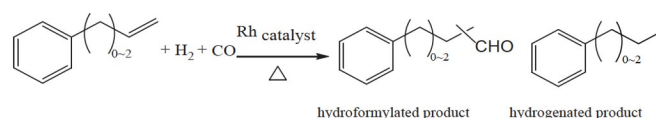


Figure 3 (A–C) EDX mapping images of $\text{Rh}_1/\text{Cs-PTA}$. (D) CO DRIFT spectra of different catalysts: $\text{Rh}/\text{K-PTA}$, $\text{Rh}/\text{Rb-PTA}$, $\text{Rh}/\text{Cs-PTA}$, and $\text{Rh}/\text{Cs-PTA}$.

aggregates of cation-PTA. According to the ICP-MS results, the Rh loading was significantly affected during the self-assembly process, which increased with the increasing precipitation rate of POM salt. The loading amount of Rh for Cs-PTA was 0.062%, higher than that for Rb-PTA (0.048%) and K-PTA (0.024%).

The hydroformylation of styrene was then conducted under different conditions (Table 1). Given that Rh loading was different for the three catalysts, TOF was calculated with respect to converted substrates per Rh site per unit time to evaluate the catalyst efficiency. Rh₁/Cs-PTA exhibited the highest TOF (1076 h⁻¹), followed by Rh₁/Rb-PTA (581 h⁻¹) and Rh₁/K-PTA (202 h⁻¹), under 2 MPa H₂/CO (1:1) at 100°C (Table S2). Thus, TOF was cation dependent. As mentioned above, the micropore size was determined by monovalent cations with different radii (Table S4). For a fast reaction such as hydroformylation, it is not unreasonable to propose that the internal mass transfer of substrates, controlled by the pore size of the catalysts, plays a role in determining the catalyst activity. In the presence of Rh₁/Cs-PTA with relatively larger pores, the mass transfer resistance was lower than that for Rh₁/Rb-PTA and Rh₁/K-PTA, resulting in higher catalytic efficiency. When allylbenzene and phenylbutene of a larger molecular size were applied as substrates, the activity obviously decreased since the allylbenzene and phenylbutene molecules had a higher resistance of mass transfer than styrene. The reusability of the catalyst was also evaluated. As shown in Figure S3, the catalyst lost its activity completely in the second run. The XRD results (Figure S4) confirmed that the Keggin structure was maintained after the reaction. However, the CO-DRIFT spectra indicated that there was no Rh remaining on the surface of the used catalyst (Figure S5). Moreover, the ICP results also confirmed that Rh was leached under hydroformylation conditions (Table S3). The hydroformylation of styrene over other metal oxide-supported catalysts was explored. CeO₂- and TiO₂-supported Rh single atoms have been investigated in previous papers (Table S5) and exhibited remarkable activity in this work (Table 1), while ZrO₂-supported Rh catalysts were found to be less active. The catalytic performance of Rh single-atom catalysts is highly dependent on the support, which plays an important role between stability and activity [62].

Table 1 Hydroformylation of styrene ^a



Catalyst	<i>n</i> -Aldehyde (%)	<i>iso</i> -Aldehyde (%)	Saturated products (%)	Conversion (%)	<i>n</i> -/ <i>iso</i> -
Rh ₁ /K-PTA	0.32	0.26	0.1	0.7	1.2
Rh ₁ /Rb-PTA	7.22	5.95	0.4	13.6	1.2
Rh ₁ /Cs-PTA	25.99	21.47	1.9	49.4	1.2
Rh ₁ /Cs-PTA ^b	6.01	5.74	0.1	11.9	1.1
Rh ₁ /Cs-PTA ^c	27.96	20.38	6.6	54.9	1.4
Rh ₁ /Cs-PTA ^d	18.50	8.50	<0.1	27.0	2.2
Rh ₁ /Cs-PTA ^e	10.12	4.90	<0.1	15.0	2.1
Rh ₁ /ZrO ₂	3.06	3.01	1.4	7.5	1.0
Rh ₁ /TiO ₂	21.36	20.66	1.53	43.5	1.0
Rh ₁ /CeO ₂	27.24	23.55	2.6	53.4	1.2

a: Otherwise stated, the conditions are: 20 mg catalyst, 2 mmol styrene, 3 mL toluene, 2 MPa H₂/CO (1:1), 100°C, 5 h. b: Temperature = 80°C. c: Temperature = 120°C. d: Substrate = allylbenzene. e: Substrate = phenylbutene.

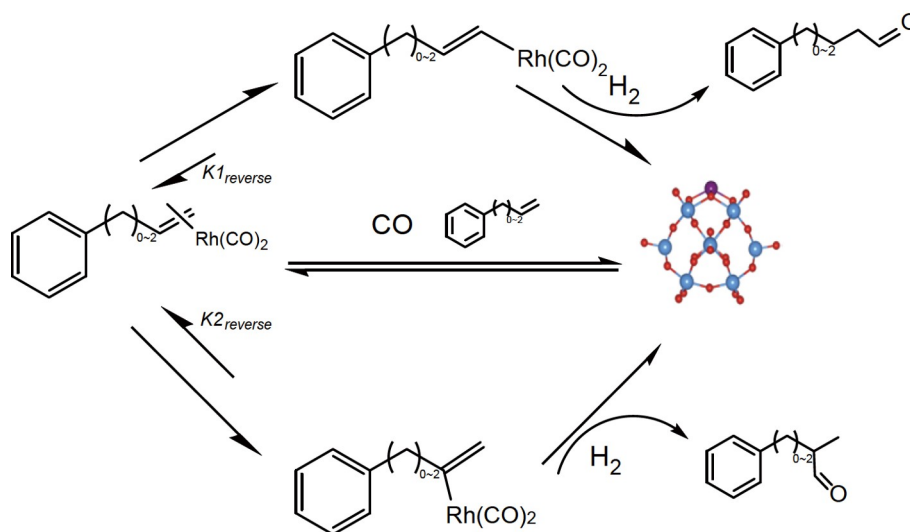
The effect of temperature was further investigated. In the presence of pressured syngas, CO molecules predominantly adsorbed on the Rh site over H₂ due to stronger interactions at low temperature (80°C) [65]. After CO insertion, the hydrogenation of the carbonyl complex led to linear and/or branched aldehydes. As the temperature increased to 120°C, the activity increased, while the hydroformylation selectivity declined due to the increasing yield of the byproduct ethylbenzene. The hydrogenation of styrene was favoured probably because CO adsorption on Rh sites was weakened at elevated temperatures. Moreover, *n*-*iso*-aldehyde was also favoured at 120°C. This might be because higher temperatures promoted the partial dissociation of the branched alkyl-rhodium intermediate, therefore preferentially enhancing $k_{2_{\text{reverse}}}$ over $k_{1_{\text{reverse}}}$ (Scheme 1), which was beneficial for the formation of *n*-aldehyde. The apparent activation energies of *n*-aldehyde and *iso*-aldehyde were further investigated. The results are shown in Figure S6. According to the exponential law of reaction rate:

$$\ln\text{TOF} = -E_a / RT + C.$$

The activation energies of *iso*-aldehyde and *n*-aldehyde were 50.4 and 74.4 kJ/mol, respectively. The higher activation energy indicated that the production of *iso*-aldehyde is more favoured at lower temperatures, while *n*-aldehyde is preferably produced at higher temperatures. Therefore, the ratio of *n*-aldehyde to *iso*-aldehyde (*n*-*iso*-) is temperature dependent. This calculation of apparent activation energy further supports the reaction routes in Scheme 1.

Based on the discussion above, a possible reaction mechanism is proposed (Scheme 1). Initially, the substrates passed through the outer surface to migrate to the enclosed Rh sites via the microslits in the aggregates and micropores present in crystals. On the Rh sites, the adsorption energy of styrene on Rh1/PTA was -4.21 eV (Figure S7). In the presence of CO, an alkyl-rhodium-carbonyl intermediate was first formed through either linear or branched coordination. After the additional CO insertion and sequential reduction by H-species, aldehyde was produced and desorbed to allocate coordination vacancies for the next styrene molecule. The major side reaction was the hydrogenation of the C=C double bond, which was favoured at high temperatures.

The leaching of Rh atoms in the POMs-supported catalyst is still a major challenge in this work. It is



Scheme 1 Reaction route of the hydroformylation of styrene and other substrates.

important to stabilize the Rh atoms without compromising activity during the practical liquid-phase hydroformylation reaction. Our previous work revealed that ILs are promising stabilizer to protect metal nanoparticles and SACs catalysts through electrostatic interaction [67,76]. For the self-assembled POMs-supported Rh catalysts, the combination of POMs and functional ILs will be investigated in the future work. The design of multi-functional ILs will be of great significance.

CONCLUSION

In this study, a porous POM salt-supported Rh single-atom catalyst was prepared to promote the hydroformylation reaction. The catalyst had three classes of structures consisting of PTA anions (primary structure), ionic crystals (secondary structure), and assembled spherical porous particles (tertiary structure). The Rh atoms were firmly coordinated onto the PTA surface within the crystals. During styrene hydroformylation, the counteraction of PTA played a key role in regulating the pore size of the catalysts, which had a substantial influence on the catalytic activity. Rh₁/Cs-PTA exhibited the highest activity (TOF = 1076 h⁻¹) compared with Rh₁/Rb-PTA and Rh₁/K-PTA, while the stereoselectivity was not altered significantly (*n*-*iso*-aldehyde = 1.2). The ratio of *n*-aldehyde to *iso*-aldehyde (*n*-*iso*-) was found to be temperature dependent. The activation energies of *iso*-aldehyde and *n*-aldehyde were 50.4 and 74.4 kJ/mol, respectively. When the temperature was increased from 80 to 100°C, the chemoselectivity of aldehydes decreased from 98.8% to 88.7%. In contrast, the stereoselectivity of the linear products was favoured and increased from 1.2 to 1.4.

Acknowledgements

We gratefully acknowledge HZWTECH for providing computation facilities. The XAS spectra were acquired at the beam-line BL01B1 at SPring-8 (Japan Synchrotron Radiation Research Institute, Hyogo, Japan) under the approval of JASRI (Proposal No. 2022B1917). We also appreciate Sikai Wang for his professional operations and analysis in conducting the EXAFS experiments.

Funding

This work was supported by the National Natural Science Foundation of China (92061109 and 22273053) and the Natural Science Basic Research Program of Shaanxi (2021JCW-20 and 2022KJXX-18).

Author contributions

N.Y. conceived the idea. N.Y. and S.F. designed the research. S.F. did the experiments. Q.Y. and X.Y. carried out the theoretical calculations. S.F. and Q.Y. co-wrote the manuscript. X.M. revised the manuscript.

Conflict of interest

The authors declare no conflict of interest.

Supplementary information

The supporting information is available online at <https://doi.org/10.1360/nso/20220064>. The supporting materials are published as submitted, without typesetting or editing. The responsibility for scientific accuracy and content remains entirely with the authors.

References

- 1 Franke R, Selent D, Börner A. Applied hydroformylation. *Chem Rev* 2012; **112**: 5675–5732.
- 2 Börner A, Franke R. *Hydroformylation: Fundamentals, Processes, and Applications in Organic Synthesis*. John Weinheim: Wiley & Sons, 2016.
- 3 Li C, Wang W, Yan L, *et al.* A mini review on strategies for heterogenization of rhodium-based hydroformylation catalysts. *Front Chem Sci Eng* 2018; **12**: 113–123.
- 4 Hanf S, Alvarado Rupflin L, Gläser R, *et al.* Current state of the art of the solid Rh-based catalyzed hydroformylation of short-chain olefins. *Catalysts* 2020; **10**: 510.
- 5 Liu B, Wang Y, Huang N, *et al.* Heterogeneous hydroformylation of alkenes by Rh-based catalysts. *Chem* 2022; **8**: 2630–2658.
- 6 Zhao K, Wang X, He D, *et al.* Recent development towards alkene hydroformylation catalysts integrating traditional homo- and heterogeneous catalysis. *Catal Sci Technol* 2022; **12**: 4962–4982.
- 7 Gao P, Liang G, Ru T, *et al.* Phosphorus coordinated Rh single-atom sites on nanodiamond as highly regioselective catalyst for hydroformylation of olefins. *Nat Commun* 2021; **12**: 4698.
- 8 Liu B, Huang N, Wang Y, *et al.* Promotion of inorganic phosphorus on Rh catalysts in styrene hydroformylation: Geometric and electronic effects. *ACS Catal* 2021; **11**: 1787–1796.
- 9 Huang N, Liu B, Lan X, *et al.* Promotion of diphosphine ligands (PPh₂(CH₂)_nPPh₂, *n* = 1, 2, 3, 5, 6) for supported Rh/SiO₂ catalysts in heterogeneous ethene hydroformylation. *Mol Catal* 2021; **511**: 111736.
- 10 Yang XF, Wang A, Qiao B, *et al.* Single-atom catalysts: A new frontier in heterogeneous catalysis. *Acc Chem Res* 2013; **46**: 1740–1748.
- 11 Wang A, Li J, Zhang T. Heterogeneous single-atom catalysis. *Nat Rev Chem* 2018; **2**: 65–81.
- 12 Hülsey MJ, Zhang J, Yan N. Harnessing the wisdom in colloidal chemistry to make stable single-atom catalysts. *Adv Mater* 2018; **30**: 1802304.
- 13 Lang R, Du X, Huang Y, *et al.* Single-atom catalysts based on the metal-oxide interaction. *Chem Rev* 2020; **120**: 11986–12043.
- 14 Li L, Chang X, Lin X, *et al.* Theoretical insights into single-atom catalysts. *Chem Soc Rev* 2020; **49**: 8156–8178.
- 15 Zhang Q, Guan J. Applications of single-atom catalysts. *Nano Res* 2022; **15**: 38–70.
- 16 Liu J. Catalysis by supported single metal atoms. *ACS Catal* 2017; **7**: 34–59.
- 17 Ding S, Hülsey MJ, Pérez-Ramírez J, *et al.* Transforming energy with single-atom catalysts. *Joule* 2019; **3**: 2897–2929.
- 18 Kaiser SK, Chen Z, Faust Akl D, *et al.* Single-atom catalysts across the periodic table. *Chem Rev* 2020; **120**: 11703–11809.
- 19 Wei H, Liu X, Wang A, *et al.* FeO_x-supported platinum single-atom and pseudo-single-atom catalysts for chemoselective hydrogenation of functionalized nitroarenes. *Nat Commun* 2014; **5**: 5634.
- 20 Zhang B, Asakura H, Zhang J, *et al.* Stabilizing a platinum₁ single-atom catalyst on supported phosphomolybdic acid without compromising hydrogenation activity. *Angew Chem* 2016; **128**: 8459–8463.
- 21 Liu W, Chen Y, Qi H, *et al.* A durable nickel single-atom catalyst for hydrogenation reactions and cellulose valorization under harsh conditions. *Angew Chem* 2018; **130**: 7189–7193.
- 22 He X, He Q, Deng Y, *et al.* A versatile route to fabricate single atom catalysts with high chemoselectivity and regioselectivity in hydrogenation. *Nat Commun* 2019; **10**: 3663.
- 23 Zhang B, Sun G, Ding S, *et al.* Atomically dispersed Pt₁-polyoxometalate catalysts: How does metal-support interaction affect stability and hydrogenation activity? *J Am Chem Soc* 2019; **141**: 8185–8197.
- 24 Zhang L, Zhou M, Wang A, *et al.* Selective hydrogenation over supported metal catalysts: From nanoparticles to single atoms. *Chem Rev* 2019; **120**: 683–733.
- 25 Long X, Li Z, Gao G, *et al.* Graphitic phosphorus coordinated single Fe atoms for hydrogenative transformations. *Nat Commun* 2020; **11**: 4074.
- 26 Yang F, Ding S, Song H, *et al.* Single-atom Pd dispersed on nanoscale anatase TiO₂ for the selective hydrogenation of

- phenylacetylene. *Sci China Mater* 2020; **63**: 982–992.
- 27 Ma Y, Zhang X, Cao L, *et al.* Effects of the morphology and heteroatom doping of CeO₂ support on the hydrogenation activity of Pt single-atoms. *Catal Sci Technol* 2021; **11**: 2844–2851.
- 28 Wang L, Zhu C, Xu M, *et al.* Boosting activity and stability of metal single-atom catalysts via regulation of coordination number and local composition. *J Am Chem Soc* 2021; **143**: 18854–18858.
- 29 Hülsey MJ, Fung V, Hou X, *et al.* Hydrogen spillover and its relation to hydrogenation: Observations on structurally defined single-atom sites. *Angew Chem Int Ed* 2022; **61**: e202208237.
- 30 Hung SF, Xu A, Wang X, *et al.* A metal-supported single-atom catalytic site enables carbon dioxide hydrogenation. *Nat Commun* 2022; **13**: 819.
- 31 Ji K, Xu M, Xu SM, *et al.* Electrocatalytic hydrogenation of 5-hydroxymethylfurfural promoted by a Ru₁Cu single-atom alloy catalyst. *Angew Chem Int Ed* 2022; **61**: e202209849.
- 32 Zhao E, Li M, Xu B, *et al.* Transfer hydrogenation with a carbon-nitride-supported palladium single-atom photocatalyst and water as a proton source. *Angew Chem Int Ed* 2022; **61**: e202207410.
- 33 Zhao L, Qin X, Zhang X, *et al.* A magnetically separable Pd single-atom catalyst for efficient selective hydrogenation of phenylacetylene. *Adv Mater* 2022; **34**: 2110455.
- 34 Xie J, Yin K, Serov A, *et al.* Selective aerobic oxidation of alcohols over atomically-dispersed non-precious metal catalysts. *ChemSusChem* 2017; **10**: 359–362.
- 35 Li T, Liu F, Tang Y, *et al.* Maximizing the number of interfacial sites in single-atom catalysts for the highly selective, solvent-free oxidation of primary alcohols. *Angew Chem Int Ed* 2018; **57**: 7795–7799.
- 36 Luo L, Luo J, Li H, *et al.* Water enables mild oxidation of methane to methanol on gold single-atom catalysts. *Nat Commun* 2021; **12**: 1218.
- 37 Shang Y, Xu X, Gao B, *et al.* Single-atom catalysis in advanced oxidation processes for environmental remediation. *Chem Soc Rev* 2021; **50**: 5281–5322.
- 38 Wang H, Jiao L, Zheng L, *et al.* PdBi single-atom alloy aerogels for efficient ethanol oxidation. *Adv Funct Mater* 2021; **31**: 2103465.
- 39 Zhang Z, Liu J, Wang J, *et al.* Single-atom catalyst for high-performance methanol oxidation. *Nat Commun* 2021; **12**: 5235.
- 40 Su X, Yang XF, Huang Y, *et al.* Single-atom catalysis toward efficient CO₂ conversion to CO and formate products. *Acc Chem Res* 2018; **52**: 656–664.
- 41 Gong L, Zhang D, Lin CY, *et al.* Catalytic mechanisms and design principles for single-atom catalysts in highly efficient CO₂ conversion. *Adv Energy Mater* 2019; **9**: 1902625.
- 42 Millet MM, Algara-Siller G, Wrabetz S, *et al.* Ni single atom catalysts for CO₂ activation. *J Am Chem Soc* 2019; **141**: 2451–2461.
- 43 Zhao C, Wang Y, Li Z, *et al.* Solid-diffusion synthesis of single-atom catalysts directly from bulk metal for efficient CO₂ reduction. *Joule* 2019; **3**: 584–594.
- 44 Li M, Wang H, Luo W, *et al.* Heterogeneous single-atom catalysts for electrochemical CO₂ reduction reaction. *Adv Mater* 2020; **32**: 2001848.
- 45 Vijay S, Ju W, Brückner S, *et al.* Unified mechanistic understanding of CO₂ reduction to CO on transition metal and single atom catalysts. *Nat Catal* 2021; **4**: 1024–1031.
- 46 Zheng T, Liu C, Guo C, *et al.* Copper-catalysed exclusive CO₂ to pure formic acid conversion via single-atom alloying. *Nat Nanotechnol* 2021; **16**: 1386–1393.
- 47 Qiao B, Wang A, Yang X, *et al.* Single-atom catalysis of CO oxidation using Pt₁/FeO_x. *Nat Chem* 2011; **3**: 634–641.
- 48 Qiao B, Liang JX, Wang A, *et al.* Single atom gold catalysts for low-temperature CO oxidation. *Chin J Catal* 2016; **37**: 1580–1586.
- 49 Nie L, Mei D, Xiong H, *et al.* Activation of surface lattice oxygen in single-atom Pt/CeO₂ for low-temperature CO oxidation. *Science* 2017; **358**: 1419–1423.

- 50 Zhang B, Asakura H, Yan N. Atomically dispersed rhodium on self-assembled phosphotungstic acid: Structural features and catalytic CO oxidation properties. *Ind Eng Chem Res* 2017; **56**: 3578–3587.
- 51 Zhang Z, Zhu Y, Asakura H, *et al.* Thermally stable single atom Pt/m-Al₂O₃ for selective hydrogenation and CO oxidation. *Nat Commun* 2017; **8**: 16100.
- 52 Hülsey MJ, Zhang B, Ma Z, *et al.* *In situ* spectroscopy-guided engineering of rhodium single-atom catalysts for CO oxidation. *Nat Commun* 2019; **10**: 1330.
- 53 Hülsey MJ, Sun G, Sautet P, *et al.* Observing single-atom catalytic sites during reactions with electrospray ionization mass spectrometry. *Angew Chem Int Ed* 2021; **60**: 4764–4773.
- 54 Hülsey MJ, Sun G, Sautet P, *et al.* Observing single-atom catalytic sites during reactions with electrospray ionization mass spectrometry. *Angew Chem* 2021; **133**: 4814–4823.
- 55 Muravev V, Spezzati G, Su YQ, *et al.* Interface dynamics of Pd-CeO₂ single-atom catalysts during CO oxidation. *Nat Catal* 2021; **4**: 469–478.
- 56 Hülsey MJ, Baskaran S, Ding S, *et al.* Identifying key descriptors for the single-atom catalyzed CO oxidation. *CCS Chem* 2022; **4**: 3296–3308.
- 57 Lu Y, Zhang Z, Wang H, *et al.* Toward efficient single-atom catalysts for renewable fuels and chemicals production from biomass and CO₂. *Appl Catal B-Environ* 2021; **292**: 120162.
- 58 De S, Burange AS, Luque R. Conversion of biomass-derived feedstocks into value-added chemicals over single-atom catalysts. *Green Chem* 2022; **24**: 2267–2286.
- 59 Ge R, Wang Y, Li Z, *et al.* Selective electrooxidation of biomass-derived alcohols to aldehydes in a neutral medium: Promoted water dissociation over a nickel-oxide-supported ruthenium single-atom catalyst. *Angew Chem Int Ed* 2022; **61**: e202200211.
- 60 Lang R, Li T, Matsumura D, *et al.* Hydroformylation of olefins by a rhodium single-atom catalyst with activity comparable to RhCl(PPh₃)₃. *Angew Chem Int Ed* 2016; **55**: 16054–16058.
- 61 Wang L, Zhang W, Wang S, *et al.* Atomic-level insights in optimizing reaction paths for hydroformylation reaction over Rh/CoO single-atom catalyst. *Nat Commun* 2016; **7**: 14036.
- 62 Amsler J, Sarma BB, Agostini G, *et al.* Prospects of heterogeneous hydroformylation with supported single atom catalysts. *J Am Chem Soc* 2020; **142**: 5087–5096.
- 63 Li T, Chen F, Lang R, *et al.* Styrene hydroformylation with *in situ* hydrogen: Regioselectivity control by coupling with the low-temperature water-gas shift reaction. *Angew Chem Int Ed* 2020; **59**: 7430–7434.
- 64 Qin T, Dang Y, Lin T, *et al.* Single-atom Ru catalyst for selective synthesis of 3-pentanone *via* ethylene hydroformylation. *Green Chem* 2021; **23**: 9038–9047.
- 65 Wei X, Jiang Y, Ma Y, *et al.* Ultralow-loading and high-performing ionic liquid-immobilizing rhodium single-atom catalysts for hydroformylation. *Chem Eur J* 2022; **28**: e202200374.
- 66 Tang P, Paganelli S, Carraro F, *et al.* Postsynthetic metalated MOFs as atomically dispersed catalysts for hydroformylation reactions. *ACS Appl Mater Interfaces* 2020; **12**: 54798–54805.
- 67 Ding S, Hülsey MJ, An H, *et al.* Ionic liquid-stabilized single-atom Rh catalyst against leaching. *CCS Chem* 2021; **3**: 1814–1822.
- 68 Kresse G, Furthmüller J. Efficient iterative schemes for *ab initio* total-energy calculations using a plane-wave basis set. *Phys Rev B* 1996; **54**: 11169–11186.
- 69 Gajdoš M, Hummer K, Kresse G, *et al.* Linear optical properties in the projector-augmented wave methodology. *Phys Rev B* 2006; **73**: 045112.
- 70 Perdew JP, Burke K, Ernzerhof M. Generalized gradient approximation made simple. *Phys Rev Lett* 1996; **77**: 3865–3868.
- 71 Blöchl PE. Projector augmented-wave method. *Phys Rev B* 1994; **50**: 17953–17979.
- 72 Mizuno N, Misono M. Heterogeneous catalysis. *Chem Rev* 1998; **98**: 199–218.
- 73 Talib SH, Yu X, Yu Q, *et al.* Non-noble metal single-atom catalysts with phosphotungstic acid (PTA) support: A

- theoretical study of ethylene epoxidation. *Sci China Mater* 2020; **63**: 1003–1014.
- 74 Brown GM, Noe-Spirlet MR, Busing WR, *et al.* Dodecatungstophosphoric acid hexahydrate, $(\text{H}_5\text{O}_2^+)_3(\text{PW}_{12}\text{O}_{40}^{3-})$. The true structure of Keggin's 'pentahydrate' from single-crystal X-ray and neutron diffraction data. *Acta Crystlogr B Struct Crystlogr Cryst Chem* 1977; **33**: 1038–1046.
- 75 Yates Jr. JT, Duncan TM, Worley SD, *et al.* Infrared spectra of chemisorbed CO on Rh. *J Chem Phys* 1979; **70**: 1219–1224.
- 76 Ding S, Guo Y, Hülsey MJ, *et al.* Electrostatic stabilization of single-atom catalysts by ionic liquids. *Chem* 2019; **5**: 3207–3219.